

TUGS: Physics-based Compact Representation of Underwater Scenes by Tensorized Gaussian

Shijie Lian^{1*}, Ziyi Zhang^{2*}, Laurence Tianruo Yang^{1,3†}, Mengyu Ren⁴, Debin Liu³, Hua Li⁴
¹Huazhong University of Science and Technology ²The Chinese University of Hong Kong, Shenzhen
³Zhengzhou University ⁴Hainan University

Abstract

Underwater 3D scene reconstruction is crucial for underwater robotic perception and navigation. However, the task is significantly challenged by the complex interplay between light propagation, water medium, and object surfaces, with existing methods unable to model their interactions accurately. Additionally, expensive training and rendering costs limit their practical application in underwater robotic systems. Therefore, we propose *Tensorized Underwater Gaussian Splatting (TUGS)*, which can effectively solve the modeling challenges of the complex interactions between object geometries and water media while achieving significant parameter reduction. TUGS employs lightweight tensorized higher-order Gaussians with a physics-based underwater Adaptive Medium Estimation (AME) module, enabling accurate simulation of both light attenuation and backscatter effects in underwater environments. Compared to other NeRF-based and GS-based methods designed for underwater, TUGS is able to render high-quality underwater images with faster rendering speeds and less memory usage. Extensive experiments on real-world underwater datasets have demonstrated that TUGS can efficiently achieve superior reconstruction quality using a limited number of parameters, making it particularly suitable for memory-constrained underwater UAV applications.

1. Introduction

Underwater 3D scene reconstruction is an essential part of perception and navigation in underwater robotics and vehicles, such as SLAM [9, 18, 27], large-scale scene reconstruction [15, 39, 42], and scene understanding [12, 31, 33]. However, reconstructing geometry in the water body is challenging due to the different properties of the water medium compared to air [23, 24, 45, 48]. Specifically, the absorption and backscatter of light in water causes signif-

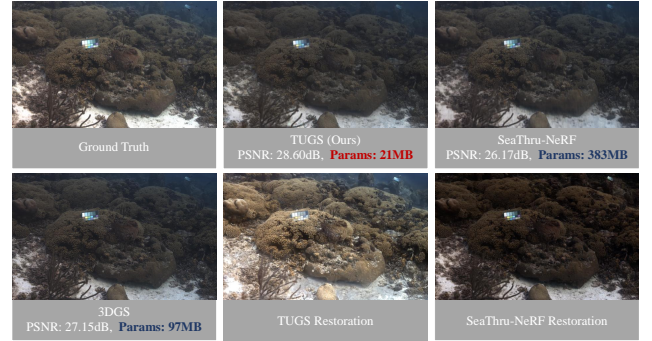


Figure 1. SeaThru-NeRF [23], 3DGS [21], and the proposed method TUGS are trained on the Curaçao scene of SeaThru-NeRF dataset. It can be seen that our model achieves the best PSNR with a size of only **21 MB**.

icant attenuation and degradation of visual content in underwater environments [1–3], causing inaccuracies in color and density estimation in 3D reconstruction methods.

In recent years, Neural Radiance Field (NeRF) [28], as a new paradigm for 3D reconstruction, enables high-quality novel view synthesis. However, the formulations of the original NeRF [28] and its follow-up variants assume that images were acquired in clear air and rendered image is composed solely of the object radiance. Specifically, the assumption of zero density between the camera and the object does not consider the absorption and scattering of light produced by different media. To address this issue, SeaThru-NeRF incorporates the water medium into the rendering model by using two radiance fields: one for the geometry and another for the water medium. However, the high training and rendering costs of SeaThru-NeRF make it challenging to synthesize high-quality images in real-time, thus limiting its practical application in underwater devices.

More recently, 3D Gaussian Splatting (3DGS) [21] introduces a new representation that models points as 3D Gaussians with learnable parameters, including 3D position, covariance, color, and opacity. However, 3DGS automatically generates a large number of dense cloudy primitives to simulate the effects of the water medium. This tends to gener-

*These authors contributed equally to this work.

†Corresponding author

ate artifacts and produces many low-opacity primitives that contribute little to the scene. This reduces rendering efficiency while significantly increasing storage costs, making it unsuitable for use in underwater vehicles and other devices with low memory.

To address the above issues, we propose the Tensorized Underwater Gaussian Splatting (TUGS), which utilizes different mode-1 slices of tensorized Gaussian to render the underwater object geometry together with the water medium. Moreover, TUGS leverages advanced tensor decomposition techniques to obtain a compact representation, significantly reducing the number of parameters required for modeling objects and water medium. As shown in Fig. 1, compared to 3DGS, TUGS uses only 20% of the parameters while maintaining a similar rendering speed. Meanwhile, SeaThru-NeRF requires 383 MB and renders at 0.09 FPS, whereas our method achieves 106 FPS with just 21 MB. This efficiency makes TUGS particularly suitable for memory-constrained underwater robotics and vehicles.

Subsequently, in order to explicitly consider the effects of the water medium in image rendering, TUGS utilizes the Adaptive Medium Estimation (AME) module to automatically estimate the corresponding light attenuation images and backscatter images of the objects in the scene and blends the previous results together to obtain the final output image through the underwater image formation model. Benefiting from the above process, TUGS does not require the generation of additional Gaussian primitives or the introduction of MLPs to adapt to the effects caused by the water medium, further reducing the amount of memory consumed. In addition, we propose a companion optimization strategy for TUGS, which consists of a tensorized densification strategy (TDS) to reduce the computational overhead of the model in the densification process, and a well-designed underwater reconstruction loss function to help the model reconstruct the underwater scene accurately and efficiently.

To validate our method, we evaluate it on the established benchmark underwater dataset, SeaThru-NeRF [23] and the simulated dataset. The results of our evaluation demonstrate the effectiveness of our proposed method in achieving high-quality, efficient underwater reconstruction. Moreover, visualization of this dataset shows that after removing the light attenuation images and backscatter images from our rendering, our model can restore the realistic colors of underwater objects and produce pleasing visual effects. In summary, we make the following contributions:

1. We propose Tensorized Underwater Gaussian Splatting (TUGS), the first framework introducing higher-order tensors into underwater 3D reconstruction to fit different parameters in underwater image formation. TUGS utilizes lightweight tensorized higher-order Gaussians to simultaneously render underwater geometry with water-induced light attenuation and backscatter while greatly

reducing the number of parameters compared to 3DGS.

2. We designed the Adaptive Medium Estimation (AME) module and corresponding optimization strategy for TUGS according to the physics-based underwater image formation model. This allows TUGS to not only accurately reconstruct the underwater scene, but also simulate the realistic colors of the image by removing the effects of the water medium.
3. Extensive experiments on the real-world dataset and simulated dataset demonstrate the effectiveness of TUGS in achieving high-quality underwater reconstruction. Meanwhile, our method has a smaller number of parameters and faster rendering speed compared to other NeRF-based and GS-based designs for underwater.

2. Related work

2.1. 3D Scene Reconstruction

3D scene reconstruction from multi-view images has long been a fundamental task in the field of computer vision. Recently, considerable attention has been paid to reconstructing 3D scenes, particularly with approaches like NeRF [28] based on implicit representation and 3DGS [21] that combine explicit and implicit representation. NeRFs [5, 6, 23, 28] model the 3D scene as a radiance field and synthesize novel views through volume rendering. Currently, NeRF has made significant advancements in various domains, such as SLAM [9, 18], large-scale scene reconstruction [15, 39, 42], dynamic scene reconstruction [32], and underwater scene reconstruction [23, 47]. SeaThru-NeRF [23] is based on the SeaThru [2] image formation model using multiple MLPs to model objects and the medium separately to address the issue of how the medium affects the appearance of objects in underwater or foggy scenes. However, due to the dense sampling and querying of NeRF’s volume rendering within multiple MLPs, the training and rendering costs are too extensive to achieve real-time rendering. In contrast, 3DGS [21] represents the scene as a set of Gaussian points and achieves real-time rendering through rasterization, demonstrating strong applicability in domains such as virtual and augmented reality (VR/AR) [20], autonomous navigation [50], and 3d scene understanding [33]. Despite these impressive advances, efficient 3D reconstruction in underwater and foggy scenes remains a challenge. In this paper, we render objects and attenuates in a lightweight way and synthesize underwater novel view results based on physical models.

2.2. Image Restoration in Scattering Media

The radiative transfer equation [10] models the interaction of light with particles in a medium, but solving it typically requires extensive Monte Carlo simulations to achieve accurate results [14, 29]. To mitigate this computational burden,

simplified models have been proposed [38, 44]. Notably, in underwater environments where medium parameters exhibit strong wavelength dependency, the SeaThru model [2, 3, 19] was introduced to address these wavelength-specific effects.

To be specific, image formation in fog, haze, or underwater differs from clear air due to two key factors: (1) the direct signal from the object is attenuated based on distance and wavelength, and (2) backscatter, or in-scattering along the line-of-sight (LOS), adds a radiance that occludes the signal. This backscatter layer is independent of the scene content but intensifies with distance, reducing visibility and contrast while distorting colors. These processes can be modeled as the following:

$$I_c(i, j) = A_c(i, j) \cdot J_c(i, j) + B_c(i, j), \quad (1)$$

where the light intensity in the channel $c \in \{R, G, B\}$ of the target along the light ray to the camera image sensor pixel (i, j) is denoted as $J_c(i, j)$ and the light intensity measured by the sensor at that pixel is denoted as $I_c(i, j)$. $A_c(i, j)$ and $B_c(i, j)$ represent wavelength-dependent light attenuation and backscatter, respectively.

However, accurate image restoration remains challenging due to the intricate interplay between light absorption and scattering in underwater environments. Traditional approaches [34, 41] have relied on multi-frame. Subsequently, single-image methods [25] are based on various image priors to restore scenes. More recently, deep learning-based methods [26, 30] have been proposed, utilizing neural networks to learn the mapping for image restoration, achieving image enhancement in underwater and foggy environments.

3. Scientific Background

3.1. Gaussian Splatting

3D Gaussian Splatting (3DGS) was first proposed to represent static scenes, which models the scene with a set of explicitly learnable Gaussians primitives $\mathbf{G} = \{\mathbf{g}_1, \mathbf{g}_2, \dots, \mathbf{g}_N\} \in \mathbb{R}^{N \times M}$, where M is the number of parameters for each Gaussian primitive. Specifically, the Gaussian primitives \mathbf{g}_i is defined by the position (mean) μ and the covariance matrix Σ [52] as follows:

$$\mathbf{g}_i(\mathbf{x}) = e^{(\mathbf{x}-\mu)^T \Sigma^{-1} (\mathbf{x}-\mu)}. \quad (2)$$

To ensure that Σ is physically meaningful, a parametric ellipsoid [51] represented by a diagonal scaling matrix \mathbf{S} and a rotation matrix \mathbf{R} is constrained to be a positive semidefinite element by defining it:

$$\Sigma = \mathbf{R} \mathbf{S} \mathbf{S}^T \mathbf{R}^T. \quad (3)$$

In practice, the parameters of each Gaussian are stored as a position vector $\mu \in \mathbb{R}^3$, a 3D scaling vector $\mathbf{s} \in \mathbb{R}^3$ and

a quaternion $\mathbf{q} \in \mathbb{R}^4$ to represent the rotation. In addition, each Gaussian is associated with an opacity $o \in \mathbb{R}$ and a color \mathbf{C}_g that are used for α -blending [28]. The color \mathbf{C}_g of the Gaussian can be either a view-dependent color computed from learned Spherical Harmonic (SH) coefficients or a learned RGB color vector. In this paper, we use the third-order SH coefficients in the RGB channel to obtain $\mathbf{C}_g \in \mathbb{R}^{(16 \times 3)}$.

The positions of the Gaussian primitives are initialized by a sparse point cloud obtained via the Stochastic Generation or Structure of Motion (SfM) algorithm [35], and optimized by successive rendering iterations with adaptive densification strategy [21] guided by the L_1 reconstruction loss and the $D - SSIM$ loss. In each rendering, the color \mathbf{C} of a pixel \mathbf{p} is computed by α -blending of intersecting Gaussians sorted by depth with o_i higher than a threshold :

$$\mathbf{C} = \sum_{i=1}^N \mathbf{c}_i \alpha_i \prod_{j=1}^i (1 - \alpha_j), \text{ and } a_i = \sigma(o_i) \cdot \hat{\mathbf{g}}_i(\mathbf{p}), \quad (4)$$

where $\hat{\mathbf{g}}_i(\mathbf{p})$ expresses whether or not the 2D projection of Gaussian \mathbf{g}_i intersects pixel \mathbf{p} .

3.2. Underwater Image Formation

In previous work [7, 17], the light attenuation $A_c(i, j)$ and the backscatter $B_c(i, j)$ during image formation with the medium are often modeled according to the atmospheric de-hazing mode [4] as:

$$A_c(i, j) = e^{-\alpha_c \cdot z(i, j)}, \quad (5)$$

$$B_c(i, j) = \gamma_c^\infty \cdot (1 - A_c(i, j)), \quad (6)$$

where the values of $\alpha_c, \gamma_c^\infty \in \mathbb{R}_{\geq 0}$ are determined by the camera system and environmental parameters, including as the medium type, target reflectance, illumination sources, image sensor characteristics, and camera depth [3].

However, when applied to underwater scenes, Eq. (5) neglects the range-dependence of underwater light attenuation coefficient α_c , and Eq. (6) incorrectly sets that the coefficients governing the range-dependence of attenuation and backscatter are the same [1]. In response, following SeaThru [2], we modeled the underwater image formation model as:

$$A_c(i, j) = e^{-f_c^\alpha(i, j) \cdot z(i, j)}, \quad (7)$$

$$B_c(i, j) = \gamma_c^\infty \cdot \left(1 - e^{-\beta_c^B \cdot z(i, j)}\right), \quad (8)$$

where scalars $\gamma_c^\infty \in \mathbb{R}_{\geq 0}$ is the backscatter color of the water at infinite distance and $\beta_c^B \in \mathbb{R}_{\geq 0}$ is the coefficient that controls backscatter. $f_c^\alpha(i, j)$ is a parametric function about light attenuation, related to depth $z(i, j)$, reflectance, ambient light, water scattering properties, and takes on different values at different pixels.

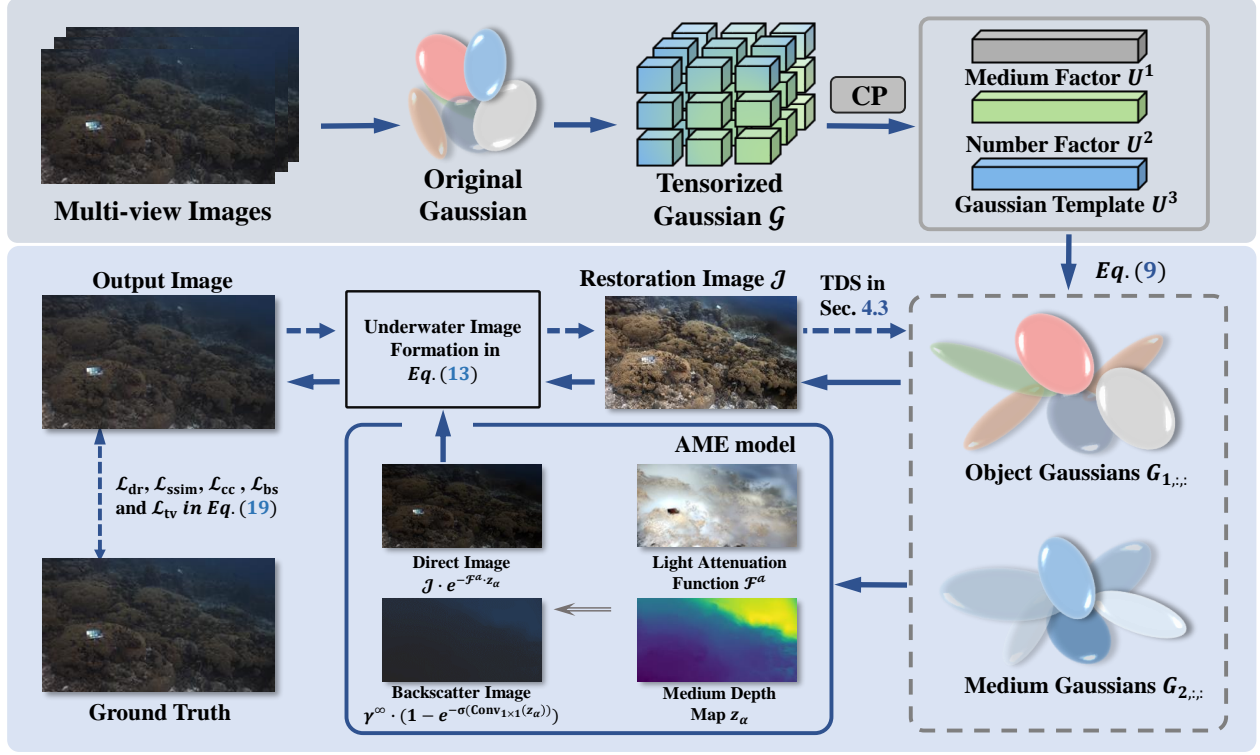


Figure 2. TUGS models the underwater object and the water medium by using different mode-1 slices of a high-order tensorized Gaussian \mathcal{G} , and simultaneously represents them using the mode factors $[\mathbf{U}^1, \mathbf{U}^2, \mathbf{U}^3]$, reducing the parameter count by approximately 60-85% compared to 3DGS [21] (in Sec. 4.1). When synthesizing images, TUGS renders the medium Gaussian as a light attenuation and backscatter image through the Adaptive Medium Estimation (AME) model and blends it with the restoration image from the object Gaussian through the underwater image formation model for the final output (in Sec. 4.2). CP is the CP decomposition [8, 16] and TDS stand for Tensorized Densification Strategies in Sec. 4.3.

4. Tensorized Underwater Gaussian Splatting

Some previous NeRF-based methods [11, 13, 36] attempted to represent the scene by constructing higher-order tensors instead of MLP-style radial fields, and then compressed parameters by decomposing these tensors into compact vector or matrix factors. Inspired by such approaches, we propose the Tensorized Underwater Gaussian Splatting (TUGS), to efficiently and accurately model underwater environments by tensor decomposition and physically-based Adaptive Medium Estimation (AME) model. Unlike previous approaches, TUGS does not directly use higher-order tensors for explicit scene representation. Instead, we construct tensorized higher-order Gaussians to render the different images required in underwater image formation. TUGS architecture can be seen in Fig. 2.

Specifically, TUGS utilizes different mode-1 slices of the tensorized Gaussian $\mathcal{G} \in \mathbb{R}^{2 \times N \times M}$ undergone CAN-DECOMP/PARAFAC (CP) tensor decomposition [8, 16] to render the underwater object geometry with the water medium. Subsequently, the Adaptive Medium Estimation (AME) module synthesizes the corresponding direct image and backscatter image of the object by Eq. (7-8). Finally,

the underwater image formation model blends the final output image from all the previous outputs, thus explicitly considering the effect of the water medium in the image rendering. In addition, we also proposed a companion optimization strategy for TUGS, which contains the Tensorized Densification Strategy (TDS) and the well-designed underwater reconstruction loss function. In the following subsections, we detail each module of the proposed method.

4.1. Tensor Decomposition

In 3DGS [21], we can directly obtain the depth $z(i, j)$ from the position of the Gaussian primitives. Thus, if we set $\gamma^\infty \in \mathbb{R}^3$ and $\beta^B \in \mathbb{R}^3$ in Eq. (8) as two learnable parameters, then we can render the target image $I_c(i, j)$ by Eq. (1) using only two sets of Gaussian to render $J_c(i, j)$ and $f_c^\alpha(i, j)$ in Eq. (7), respectively. This allows us to represent the underwater scene with a tensorized Gaussians $\mathcal{G} \in \mathbb{R}^{2 \times N \times M}$.

Furthermore, to reduce the number of parameters in \mathcal{G} and represent it in a more compact form, we apply CP tensor decomposition to \mathcal{G} . This decomposition breaks it down into three factor matrices: the medium factor $\mathbf{U}^1 \in \mathbb{R}^{2 \times R}$, the number factor $\mathbf{U}^2 \in \mathbb{R}^{N \times R}$ and the Gaussian template

$\mathbf{U}^3 \in \mathbb{R}^{M \times R}$, where R is the selected rank of the decomposition. Specifically, we can represent the tensorized Gaussians \mathcal{G} as:

$$\mathcal{G} \approx \sum_{r=1}^R \mathbf{u}_{:,r}^1 \circ \mathbf{u}_{:,r}^2 \circ \mathbf{u}_{:,r}^3, \quad (9)$$

where \circ represents the vector outer product, $\mathbf{u}_{:,r}^m$ is the r -th column of \mathbf{U}^m . During training, we only learn the matrices \mathbf{U}^1 , \mathbf{U}^2 , \mathbf{U}^3 and use the mode-1 slices $\mathbf{G}_{1,:}$ and $\mathbf{G}_{2,:}$ to render $J_c(i, j)$ and $f_c^\alpha(i, j)$ respectively.

Benefiting from tensorized Gaussians, the parametric cost of introducing an extra set of Gaussian primitives for rendering $f_c^\alpha(i, j)$ is reduced from $M \times N$ to R . Moreover, since R is smaller than M and N , the total number of parameters for TUGS, $(M + N + 2) \times R$, is smaller than the total number of parameters for the original 3DGS (MN). For instance, when $R = 20$, $N = 2 \times 10^5$, and $M = 59$, TUGS learns only $(M + N + 2) \times R \approx 4 \times 10^6$ parameters, compared to $MN = 12 \times 10^6$ that original 3DGS representations would require, **thus reducing the total number of learnable parameters by about 66%**. This makes our method more suitable for memory-constrained underwater robotics and vehicles than existing 3DGS-based and NeRF-based methods.

4.2. Adaptive Medium Estimation and Formation

In the previous subsection, we obtained the clean underwater image \mathcal{J} with the light attenuation function \mathcal{F}^α . Then, we'll blend them into the final output through the Adaptive Medium Estimation (AME) module. Specifically, for a given camera direction d , \mathcal{J} and \mathcal{F}^α with depth \mathbf{z} will can be rendered as:

$$\mathcal{J}, \mathbf{z}_u = r(\mathbf{G}_{1,:}, d), \quad (10)$$

$$\mathcal{F}^\alpha, \mathbf{z}_\alpha = r(\mathbf{G}_{2,:}, d), \quad (11)$$

where $\mathcal{J}, \mathcal{F}^\alpha \in \mathbb{R}^{H \times W \times 3}$ and $\mathbf{z}_u, \mathbf{z}_\alpha \in \mathbb{R}^{H \times W}$, $r(\mathbf{G}, d)$ is the differentiable rasterization of Gaussian \mathbf{G} at camera direction d . Subsequently, we estimate the backscatter image $\mathcal{B} \in \mathbb{R}^{H \times W \times 3}$ based on Eq. (8), and the backscatter coefficient β^B is modeled using a 1×1 convolution layer $\text{Conv}_{1 \times 1}(\cdot)$, where the layer's weights are denoted as $\mathcal{W} \in \mathbb{R}^{1 \times 3 \times 1 \times 1}$. Consequently, \mathcal{B} is expressed as:

$$\mathcal{B} = \gamma^\infty \cdot \left(1 - e^{-\sigma(\text{Conv}_{1 \times 1}(\mathbf{z}_\alpha))}\right), \quad (12)$$

where γ^∞ is a non-negative learnable variable and $\sigma(\cdot)$ denotes the ReLU activation function. Then, the image $\mathbf{I} \in \mathbb{R}^{H \times W \times 3}$, synthesized based on the underwater image formation model, can be rendered as follows:

$$\mathbf{I} = \mathcal{J} \cdot e^{-\mathcal{F}^\alpha \cdot \mathbf{z}_\alpha} + \mathcal{B}. \quad (13)$$

In addition, in order to make the Gaussian primitive that renders the light attenuation more focused on the information related to the scattering of the water body, we use \mathbf{z}_α instead of \mathbf{z}_u in Eq. (12) and Eq. (13).

4.3. Tensorized Denisfication Strategies

During the optimization of 3DGS, a set of Gaussian points undergo an adaptive density control strategy, allowing the dynamic addition and removal of individual Gaussians. However, when using TUGS, operations such as segmentation of oversized Gaussians lead to multiple CP decompositions and tensor composition operations at each adaptive density control, introducing unnecessary computational overhead to the model. Therefore, we redesign a tensorized denisfication strategy based on the characteristics of tensorized Gaussian. Our tensorized denisfication strategy consists of three simple steps, adding Gaussians based on gradient, pruning Gaussians based on opacity, and zeroing opacity periodically.

In contrast to the original 3DGS, we do not determine whether a Gaussian primitive is too large or too small, nor do we split the Gaussian primitive. For all Gaussian primitive with gradients larger than the threshold t_g , we make a copy of their corresponding number factor \mathbf{U}^2 and initialize the optimizer parameters of the added part to zero, while the original copied part retains the gradient information. In this way, TUGS only needs to add R parameters to represent a new Gaussian primitive. Subsequently, we eliminate the Gaussian primitives that contribute poorly to the scene by removing the Gaussian primitives whose opacity is lower than the threshold t_o , specifically, the retained primitives can be denoted as:

$$\mathbf{U}_{\text{retain}}^2 = \left\{ \mathbf{u}_{i,:}^2 | \mathbf{u}_{i,:}^2 (\mathbf{u}_{\alpha,:}^3 \odot \mathbf{u}_{1,:}^1)^T \geq t_o \right\} \quad (14)$$

where \odot is the Khatri–Rao product [37] and $\mathbf{u}_{\alpha,:}^3$ is the row of the Gaussian Template \mathbf{U}^3 that represents opacity. In this way, instead of a complete reduction of the tensor back to its original Gaussian form, we only need to perform a minimal unfolding to compute the opacity of each Gaussian primitive representing the underwater geometry and filter it from there. And during the periodic zeroing of opacity, we simply set $\mathbf{u}_{\alpha,:}^3 = \mathbf{0}$. With the above steps, we can minimize the memory usage and computational requirements in Tensorized Denisfication Strategies.

4.4. Underwater Reconstruction Loss Function

In contrast to 3D reconstruction in clear-air scenes, underwater 3D reconstruction must explicitly consider the effects of the underwater medium's scattering and attenuation of light, and simultaneously learn information such as depth and the underwater object's original color. Therefore, we introduce color correction loss, backscatter loss, and depth-weighted reconstruction loss to effectively supervise the underwater challenges.

Similar to other underwater color correction works [2, 19], we encourage the average values of each color channel in restoration image \mathcal{J} to approach the middle of the

Method	IUI3 Red Sea				Curaçao				J.G. Red Sea				Panama				Avg.
	PSNR	SSIM	LPIPS	Storage	PSNR	SSIM	LPIPS	Storage	PSNR	SSIM	LPIPS	Storage	PSNR	SSIM	LPIPS	Storage	FPS
SeaThru-NeRF [23]	25.84	0.85	0.30	383 MB	26.17	0.81	0.28	383 MB	21.09	0.76	0.29	383 MB	27.04	0.85	0.22	383 MB	0.09
TensoRF [11]	17.33	0.55	0.63	66 MB	23.38	0.79	0.45	66 MB	15.19	0.51	0.59	66 MB	20.76	0.75	0.38	66 MB	0.21
3DGS [21]	28.28	0.86	0.26	105 MB	27.15	0.85	0.25	97 MB	20.26	0.82	0.23	89 MB	30.23	0.89	0.19	75 MB	154.9
SeaSplat [48]	26.47	0.85	0.28	140 MB	27.79	0.86	0.27	129 MB	19.21	0.70	0.35	138 MB	29.79	0.88	0.19	104 MB	80.7
UW-GS [45]	27.06	0.84	0.27	78 MB	27.62	0.87	0.25	64 MB	20.05	0.71	0.32	68 MB	31.36	0.90	0.17	61 MB	78.6
TUGS ($R = 20$)	28.98	0.86	0.26	18 MB	28.60	0.88	0.23	21 MB	22.21	0.84	0.23	11 MB	31.27	0.90	0.18	12 MB	106.7
TUGS ($R = 30$)	29.36	0.87	0.25	31 MB	28.71	0.87	0.22	43 MB	22.43	0.86	0.22	37 MB	31.51	0.92	0.16	34 MB	82.1

Table 1. Quantitative evaluation on the SeaThru-NeRF dataset, where R stand for rank in mode factors $[\mathbf{U}^1, \mathbf{U}^2, \mathbf{U}^3]$. We show the PSNR \uparrow , SSIM \uparrow , and LPIPS \downarrow . Light red and light yellow correspond to the first and second.

color range and expect its standard deviation to be similar to the direct signal $\mathcal{D} = \mathcal{G} - \mathcal{B}$, where \mathcal{G} is the ground truth. Therefore, the color correction loss \mathcal{L}_{cc} is defined as:

$$\mathcal{L}_{cc} = \sum_c \left((m(\mathbf{J}_c) - 0.5)^2 + (s(\mathbf{J}_c) - s(\mathbf{D}_c))^2 \right), \quad (15)$$

where color $c \in \{R, G, B\}$, $m(\cdot)$ and $s(\cdot)$ are used to calculate the mean and standard deviation. We also optimized the backscatter images using the backscatter loss developed by DeepSeeColor [19], which is a variant of the dark channel prior loss [17]:

$$\mathcal{L}_{bs} = \sum_c \sum_{(i,j)} (\sigma(D_c(i,j)) + k \cdot \sigma(-D_c(i,j))), \quad (16)$$

where $\sigma(\cdot)$ denotes the ReLU activation function and hyperparameter $k = 1000$.

In addition, since light attenuation and backscatter are potentially the most significant effects on the distant objects, we give the higher weight to the distant pixel regions in the original 3DGS L_1 loss, and thus propose a depth-weighted reconstruction L_1 loss:

$$\mathcal{L}_{dr} = \sum_c \sum_{(i,j)} z_u(i,j) \cdot |G_c(i,j) - I_c(i,j)|, \quad (17)$$

where \mathbf{z}_u is the scene depth calculated by Eq. (10). At the same time, we regularize the estimated depth \mathbf{z}_u and \mathbf{z}_α to make the depth map predicted by the network smoother. The specific formula is as follows:

$$\mathcal{L}_{tv} = \sum_{\mathbf{z} \in \{\mathbf{z}_u, \mathbf{z}_\alpha\}} TV(z), \quad (18)$$

where $TV(\cdot)$ is the total variation loss [43]. In summary, our total losses are as follows:

$$\mathcal{L} = \lambda_1 \mathcal{L}_{dr} + \lambda_2 \mathcal{L}_{ssim} + \lambda_3 \mathcal{L}_{cc} + \lambda_4 \mathcal{L}_{bs} + \lambda_5 \mathcal{L}_{tv} \quad (19)$$

where \mathcal{L}_{ssim} corresponding to the D-SSIM loss in original 3D Gaussian Splatting [21], $\lambda_1, \lambda_2, \lambda_3, \lambda_4$, and λ_5 is the hyperparameter that balances the different loss functions. In this paper, except for λ_1 and λ_2 , which are set to 0.8 and 0.2 based on 3DGS, all others are set to 1.

5. Experiments

5.1. Implementation and Optimization

We implement our method based on the code of 3D Gaussian Splatting [21], and implement the tensor decomposition operation through the TensorLy package [22]. For initialization, in order to simplify the computation as much as possible, we only use the underwater scene to initialize the object Gaussian $\mathbf{G}_{1,:}$ and initialize the medium Gaussian $\mathbf{G}_{2,:}$ by a simple copy operation. Specifically, we apply the original initialization method of 3DGS to obtain the set of initial Gaussians and add a dimension to it, transforming it into the $\mathcal{G}_{init}^{1 \times H \times W}$, and apply the CP tensor decomposition to split it into $\mathbf{U}_{init}^1 \in \mathbb{R}^{1 \times R}$, $\mathbf{U}_{init}^2 \in \mathbb{R}^{N \times R}$ and $\mathbf{U}_{init}^3 \in \mathbb{R}^{M \times R}$. Finally, we complete our initialization by making a copy of \mathbf{U}_{init}^1 and changing it to $\mathbf{U}_{copy}^1 \in \mathbb{R}^{2 \times R}$. We used the Adam optimizer to train our TUGS on RTX 4090 GPUs for the 20,000 step, and the learning rates and hyperparameters of all the optimizers remained consistent with the original 3DGS [21].

In addition, The initial value of learnable parameter λ^∞ is empirically set to $[0.1, 0.2, 0.3]$. The convolutional layer used in Eq. (12) uses the uniform initialization. The convolutional layer and λ^∞ are used with the Adam optimizer, and their initial learning rate is set to 10^{-3} . For the Tensorized Densification Strategies, we set the gradient threshold t_g for copying new Gaussians to 10^{-3} and the opacity threshold t_o for removal of low-opacity Gaussians to 0.1. Additionally, we reset the opacity of the Gaussian tuples to zero every 1,000 steps. The Tensorized Densification Strategies will continue for 10,000 steps to help TUGS generate sufficient and reasonable Gaussians for the reconstruction of the underwater scene.

5.2. Dataset

SeaThru-NeRF Dataset. The SeaThru-NeRF dataset, introduced in [23], comprises real-world scenes from four distinct underwater locations: IUI3 Red Sea, Curaçao, Japanese Garden Red Sea, and Panama. The dataset includes 29, 20, 20, and 18 images for each location, with 25, 17, 17, and 15 images allocated for training, and the re-

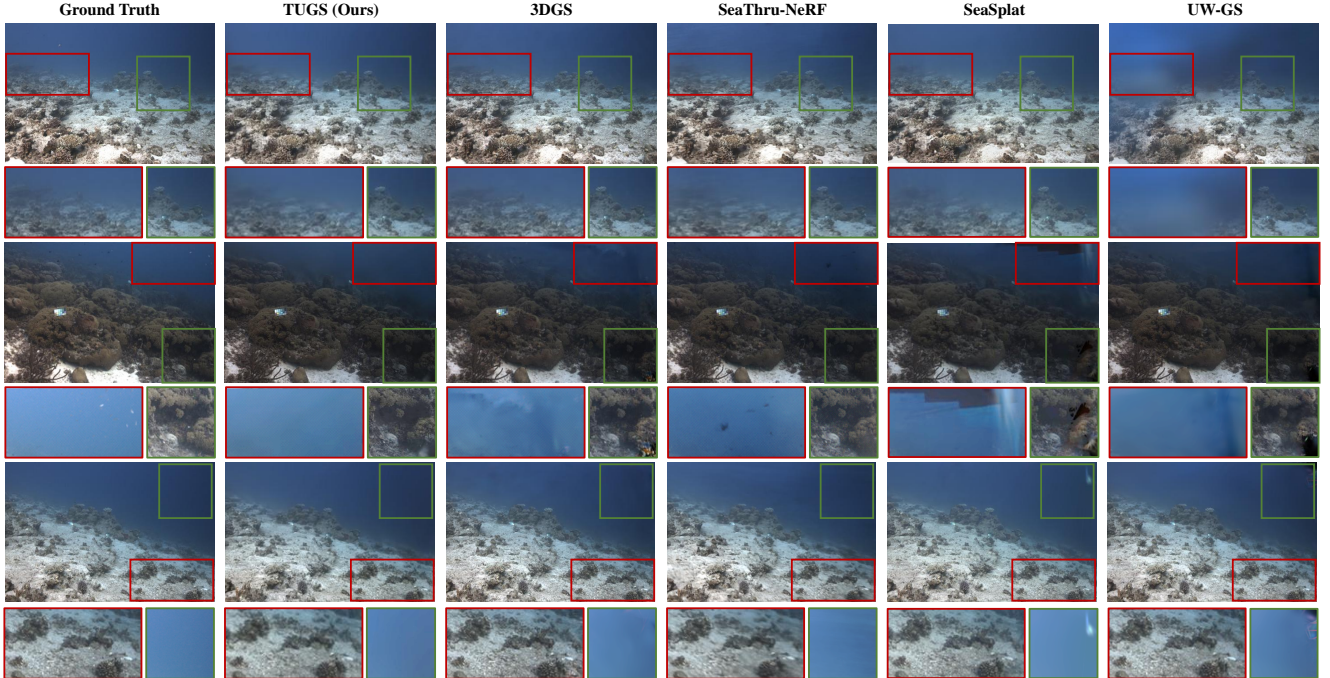


Figure 3. Novel view rendering comparisons in SeaThru-NeRF dataset [23]. We adjusted the image brightness of two highlighted regions in row 4 and the green highlighted region in row 6 with the same settings for more visual comparisons of the different methods.

Method	PSNR	SSIM	LPIPS	Storage
SeaThru-NeRF [23]	20.07	0.66	0.61	383 MB
3DGS [21]	18.94	0.61	0.69	135 MB
TUGS ($R = 30$)	23.64	0.74	0.53	58 MB

Table 2. Quantitative evaluation on the simulated dataset.

maining 4, 3, 3, and 3 images reserved for validation. This dataset captures different water conditions and imaging scenarios, providing a comprehensive benchmark for underwater scene reconstruction.

Simulated Dataset. To further evaluate the performance of the proposed method, we used the bicycle scene from the Mip-NeRF 360 dataset [5] and added fog to it to simulate the presence of the medium follow SeaThru-NeRF [23].

5.3. Baseline methods and Evaluation Metrics

To ensure fairness, the input to all methods is the same set of white-balanced linear images. For rendering scenes with the medium, we compare the SeaThru-NeRF [40], TensorRF [11], 3DGS [21], SeaSplat [48], and UW-GS [45]. As shown in Tab. 1, we evaluate the model performance by calculating the PSNR, SSIM [46], and LPIPS [49] to compare the rendering effect between different models. We also evaluated the parameters needed to represent the same scene for TUGS and the above models. In the task of reconstructing clean medium-free images, since we do not have ground truth images without the water medium, we follow the setup of SeaThru [2] and show the results of the visual

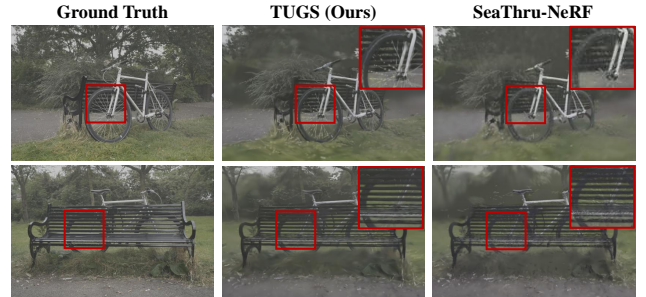


Figure 4. Synthesizing novel views in a foggy environment.

comparison with the SeaSplat and UW-GS in Fig. 5.

5.4. Results

First, Tab. 1 shows that TUGS requires only 13-45% of the number of parameters of 3DGS to present a leading position in most scenarios and metrics. And even compared to SeaThru-NeRF, which has about 10-20 times the number of parameters, we can present a leading position in all metrics. For TensorRF [11], which also uses Tensor decomposition to compress the scene, the rendered image shows excessive smoothing and fails to achieve satisfactory results due to its inability to properly model the relationship between the underwater object and the medium.

Additionally, as shown in the red-highlighted areas of the first row in Fig. 3, UW-GS [45], a Gaussian Splatting method specifically designed for underwater environments, exhibits noticeable artifacts when rendering water. In the

Method	PSNR	SSIM	LPIPS
TG	26.80	0.79	0.43
TG + AME	27.24	0.81	0.40
TG + AME + Loss	27.78	0.83	0.33
TG + AME + Loss + TDS	29.36	0.87	0.25

Table 3. Ablations experiments for each component of TUGS. TG denotes tensorized Gaussian, AME denotes adaptive medium estimation, Loss is our loss function defined in Eq. (19), and TDS is our tensorized densification strategy.

third row, the red-highlighted area reveals unnatural gaps in the background of the image synthesized by SeaSplat [48]. In contrast, our method utilizes the AME module to properly blend the restoration image, light attenuation, and backscatter, producing the final output with visually satisfactory results.

Moreover, it can be seen in Tab. 2 and Fig. 4 that the same advantages of our method are observed in the simulated dataset. It outperforms SeaThru-NeRF in fogged images and all types of metrics.

5.5. Ablations

We decompose the components of TUGS and validate the effectiveness of each module through incremental additions. All ablation experiments are conducted on the IUI3 Red Sea scene from the SeaThru-NeRF dataset [23], with the CP decomposition rank set to 30. As shown in Tab. 3, initially, when we simply apply CP decomposition to the parameters of 3DGS and remove the original densification, the model’s performance experiences a decline compared to 3DGS. However, when we introduce our adaptive medium estimation module and underwater loss function, the model demonstrates a significant performance improvement.

Notably, without the densification strategy, the model TG + AME + Loss typically contains around 20,000 Gaussian primitives (approximately 3MB), which results in exceptionally fast training speed and minimal memory requirements. This configuration is well-suited for deployment on resource-constrained underwater edge devices. Furthermore, after incorporating our tensorized densification strategy, the model’s performance improves considerably, enabling precise underwater scene modeling with only about 29.5% of the parameters of 3DGS.

6. Limitations

Although our method achieves high reconstruction quality with a small number of parameters and performs better in speed compared to other GS-based and NeRF-based methods designed for underwater environments, it also has some limitations that need to be considered. First, like SeaSplat [48] and UW-GS [45], our method encounters difficulties in separating background objects from the medium, as shown

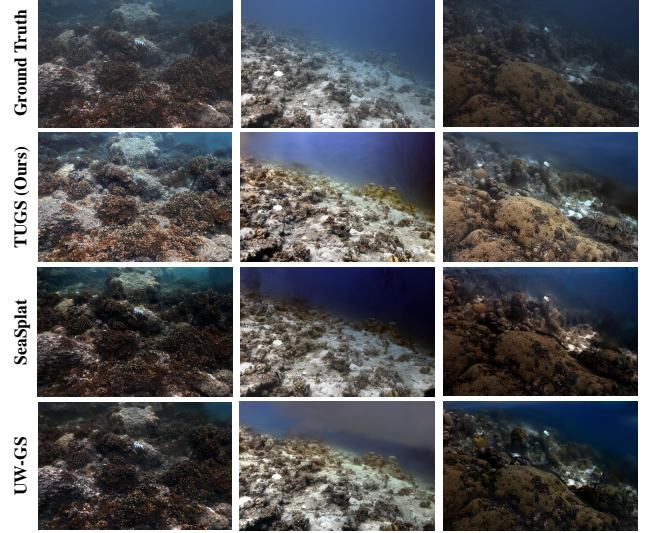


Figure 5. Novel view synthesis without water media in the SeaThru NeRF dataset [23]. TUGS restores the underlying colors of the scene more vividly and foreground details are clearer.

in the first and third columns of Fig. 5. This is mainly due to the fact that under the influence of the medium, the color of the background object and the backscatter become entangled during training. However, our model consistently performs well in the foreground. For example, in the green-highlighted area of the fourth row in Fig. 3, 3DGS, SeaSplat, and UW-GS all exhibit noticeable artifacts in the scene, whereas our rendering does not. Additionally, due to the lack of ground truth images with the water medium completely removed, it is not possible to directly supervise the restoration process. As a result, like other methods, our approach cannot guarantee completely accurate color reconstruction. Nevertheless, we introduce color correction loss and backscatter loss (Eqs. (15) and (16)) to ensure that colors are restored as reasonably as possible.

7. Conclusion

In this work, we introduce Tensor Underwater Gaussian Stitching (TUGS), the first framework for underwater 3D reconstruction that enables high-quality rendering in complex underwater environments. TUGS utilizes tensorized Gaussians and physically-based Adaptive Medium Estimation (AME) modules to efficiently capture the intricate interactions between the water medium and the object geometry, without the excessive parameter overhead of previous methods. By explicitly modeling underwater image formation, TUGS achieves a remarkable balance between high fidelity and parameter compactness, making it ideally suited for resource-limited underwater robotics applications.

References

- [1] Derya Akkaynak and Tali Treibitz. A revised underwater image formation model. In *CVPR*, 2018. 1, 3
- [2] Derya Akkaynak and Tali Treibitz. Sea-thru: A method for removing water from underwater images. In *CVPR*, 2019. 2, 3, 5, 7
- [3] Derya Akkaynak, Tali Treibitz, Tom Shlesinger, Yossi Loya, Raz Tamir, and David Iluz. What is the space of attenuation coefficients in underwater computer vision? In *CVPR*, pages 4931–4940, 2017. 1, 3
- [4] Shunmin An, Xixia Huang, Lujia Cao, and Linling Wang. A comprehensive survey on image dehazing for different atmospheric scattering models. *Multimedia Tools and Applications*, 83(14):40963–40993, 2024. 3
- [5] Jonathan T Barron, Ben Mildenhall, Dor Verbin, Pratul P Srinivasan, and Peter Hedman. Mip-nerf 360: Unbounded anti-aliased neural radiance fields. In *CVPR*, pages 5470–5479, 2022. 2, 7
- [6] Jonathan T. Barron, Ben Mildenhall, Dor Verbin, Pratul P. Srinivasan, and Peter Hedman. Zip-nerf: Anti-aliased grid-based neural radiance fields. In *ICCV*, pages 19697–19705, 2023. 2
- [7] Dana Berman, Tali treibitz, and Shai Avidan. Non-local image dehazing. In *CVPR*, 2016. 3
- [8] J Douglas Carroll and Jih-Jie Chang. Analysis of individual differences in multidimensional scaling via an n-way generalization of “eckart-young” decomposition. *Psychometrika*, 35(3):283–319, 1970. 4
- [9] Vincent Cartillier, Grant Schindler, and Irfan Essa. Slaim: Robust dense neural slam for online tracking and mapping. In *Proceedings of the IEEE/CVF Conference on Computer Vision and Pattern Recognition*, pages 2862–2871, 2024. 1, 2
- [10] Subrahmanyam Chandrasekhar. *Radiative transfer*. Courier Corporation, 2013. 2
- [11] Anpei Chen, Zexiang Xu, Andreas Geiger, Jingyi Yu, and Hao Su. Tensorf: Tensorial radiance fields. In *ECCV*, pages 333–350. Springer, 2022. 4, 6, 7
- [12] Runnan Chen, Youquan Liu, Lingdong Kong, Xinge Zhu, Yuexin Ma, Yikang Li, Yuenan Hou, Yu Qiao, and Wenping Wang. Clip2scene: Towards label-efficient 3d scene understanding by clip. In *Proceedings of the IEEE/CVF Conference on Computer Vision and Pattern Recognition*, pages 7020–7030, 2023. 1
- [13] Sara Fridovich-Keil, Giacomo Meanti, Frederik Rahbæk Warburg, Benjamin Recht, and Angjoo Kanazawa. K-planes: Explicit radiance fields in space, time, and appearance. In *CVPR*, pages 12479–12488, 2023. 4
- [14] Iliyan Georgiev, Jaroslav Krivanek, Toshiya Hachisuka, Derek Nowrouzezahrai, and Wojciech Jarosz. Joint importance sampling of low-order volumetric scattering. *ACM Trans. Graph.*, 32(6):164–1, 2013. 2
- [15] Jiaming Gu, Minchao Jiang, Hongsheng Li, Xiaoyuan Lu, Guangming Zhu, Syed Afaq Ali Shah, Liang Zhang, and Mohammed Bennisamoun. Ue4-nerf: Neural radiance field for real-time rendering of large-scale scene. *Advances in Neural Information Processing Systems*, 36, 2024. 1, 2
- [16] Richard A Harshman et al. Foundations of the parafac procedure: Models and conditions for an “explanatory” multi-modal factor analysis. *UCLA Working Papers in Phonetics*, 16, 1970. 4
- [17] Kaiming He, Jian Sun, and Xiaoou Tang. Single image haze removal using dark channel prior. In *CVPR*, pages 1956–1963, 2009. 3, 6
- [18] Tongyan Hua and Lin Wang. Benchmarking implicit neural representation and geometric rendering in real-time rgb-d slam. In *Proceedings of the IEEE/CVF Conference on Computer Vision and Pattern Recognition*, pages 21346–21356, 2024. 1, 2
- [19] Stewart Jamieson, Jonathan P. How, and Yogesh Girdhar. Deepseecolor: Realtime adaptive color correction for autonomous underwater vehicles via deep learning methods. In *ICRA*, pages 3095–3101, 2023. 3, 5, 6
- [20] Ying Jiang, Chang Yu, Tianyi Xie, Xuan Li, Yutao Feng, Huamin Wang, Minchen Li, Henry Lau, Feng Gao, Yin Yang, et al. Vr-gs: A physical dynamics-aware interactive gaussian splatting system in virtual reality. In *ACM SIGGRAPH 2024 Conference Papers*, pages 1–1, 2024. 2
- [21] Bernhard Kerbl, Georgios Kopanas, Thomas Leimkuehler, and George Drettakis. 3d gaussian splatting for real-time radiance field rendering. *ACM TOG*, 42(4), 2023. 1, 2, 3, 4, 6, 7
- [22] Jean Kossaifi, Yannis Panagakis, Anima Anandkumar, and Maja Pantic. Tensorly: Tensor learning in python. *JMLR*, 20(26):1–6, 2019. 6
- [23] Deborah Levy, Amit Peleg, Naama Pearl, Dan Rosenbaum, Derya Akkaynak, Simon Korman, and Tali Treibitz. Seathru-nerf: Neural radiance fields in scattering media. In *CVPR*, pages 56–65, 2023. 1, 2, 6, 7, 8
- [24] Huapeng Li, Wenxuan Song, Tianao Xu, Alexandre Elsig, and Jonas Kulhanek. WaterSplatting: Fast Underwater 3D Scene Reconstruction Using Gaussian Splatting. *arXiv e-prints*, art. arXiv:2408.08206, 2024. 1
- [25] Yu Li, Shaodi You, Michael S Brown, and Robby T Tan. Haze visibility enhancement: A survey and quantitative benchmarking. *Computer Vision and Image Understanding*, 165:1–16, 2017. 3
- [26] Risheng Liu, Xin Fan, Ming Zhu, Minjun Hou, and Zhongxuan Luo. Real-world underwater enhancement: Challenges, benchmarks, and solutions under natural light. *IEEE transactions on circuits and systems for video technology*, 30(12):4861–4875, 2020. 3
- [27] Andréa Macario Barros, Maugan Michel, Yoann Moline, Gwenolé Corre, and Frédéric Carrel. A comprehensive survey of visual slam algorithms. *Robotics*, 11(1):24, 2022. 1
- [28] Ben Mildenhall, Pratul P Srinivasan, Matthew Tancik, Jonathan T Barron, Ravi Ramamoorthi, and Ren Ng. Nerf: Representing scenes as neural radiance fields for view synthesis. *ECCV*, pages 405–421, 2020. 1, 2, 3
- [29] Jan Novák, Iliyan Georgiev, Johannes Hanika, and Wojciech Jarosz. Monte carlo methods for volumetric light transport simulation. In *Computer graphics forum*, pages 551–576. Wiley Online Library, 2018. 2

- [30] Lintao Peng, Chunli Zhu, and Liheng Bian. U-shape transformer for underwater image enhancement. *IEEE Transactions on Image Processing*, 32:3066–3079, 2023. 3
- [31] Songyou Peng, Kyle Genova, Chiyu Jiang, Andrea Tagliasacchi, Marc Pollefeys, Thomas Funkhouser, et al. Openscene: 3d scene understanding with open vocabularies. In *Proceedings of the IEEE/CVF conference on computer vision and pattern recognition*, pages 815–824, 2023. 1
- [32] Albert Pumarola, Enric Corona, Gerard Pons-Moll, and Francesc Moreno-Noguer. D-nerf: Neural radiance fields for dynamic scenes. In *Proceedings of the IEEE/CVF Conference on Computer Vision and Pattern Recognition*, pages 10318–10327, 2021. 2
- [33] Minghan Qin, Wanhua Li, Jiawei Zhou, Haoqian Wang, and Hanspeter Pfister. Langsplat: 3d language gaussian splatting. In *Proceedings of the IEEE/CVF Conference on Computer Vision and Pattern Recognition*, pages 20051–20060, 2024. 1, 2
- [34] Yoav Y Schechner, Srinivasa G Narasimhan, and Shree K Nayar. Instant dehazing of images using polarization. In *Proceedings of the 2001 IEEE Computer Society Conference on Computer Vision and Pattern Recognition. CVPR 2001*, pages I–I. IEEE, 2001. 3
- [35] Johannes L. Schonberger and Jan-Michael Frahm. Structure-from-motion revisited. In *CVPR*, 2016. 3
- [36] Ruizhi Shao, Zerong Zheng, Hanzhang Tu, Boning Liu, Hongwen Zhang, and Yebin Liu. Tensor4d: Efficient neural 4d decomposition for high-fidelity dynamic reconstruction and rendering. In *Proceedings of the IEEE/CVF Conference on Computer Vision and Pattern Recognition*, pages 16632–16642, 2023. 4
- [37] Age K Smilde, Rasmus Bro, and Paul Geladi. *Multi-way analysis: applications in the chemical sciences*. John Wiley & Sons, 2005. 5
- [38] Bo Sun, Ravi Ramamoorthi, Srinivasa G Narasimhan, and Shree K Nayar. A practical analytic single scattering model for real time rendering. *ACM Transactions on Graphics (TOG)*, 24(3):1040–1049, 2005. 3
- [39] Matthew Tancik, Vincent Casser, Xincheng Yan, Sabeek Pradhan, Ben Mildenhall, Pratul P Srinivasan, Jonathan T Barron, and Henrik Kretzschmar. Block-nerf: Scalable large scene neural view synthesis. In *Proceedings of the IEEE/CVF Conference on Computer Vision and Pattern Recognition*, pages 8248–8258, 2022. 1, 2
- [40] Matthew Tancik, Ethan Weber, Evonne Ng, Ruilong Li, Brent Yi, Terrance Wang, Alexander Kristoffersen, Jake Austin, Kamyar Salahi, Abhik Ahuja, David Mcallister, Justin Kerr, and Angjoo Kanazawa. Nerfstudio: A modular framework for neural radiance field development. In *ACM SIGGRAPH 2023 Conference Proceedings*, New York, NY, USA, 2023. Association for Computing Machinery. 7
- [41] Tali Treibitz and Yoav Y Schechner. Active polarization descattering. *IEEE transactions on pattern analysis and machine intelligence*, 31(3):385–399, 2008. 3
- [42] Haithem Turki, Deva Ramanan, and Mahadev Satyanarayanan. Mega-nerf: Scalable construction of large-scale nerfs for virtual fly-throughs. In *Proceedings of the IEEE/CVF Conference on Computer Vision and Pattern Recognition*, pages 12922–12931, 2022. 1, 2
- [43] C. R. Vogel and M. E. Oman. Iterative methods for total variation denoising. *SIAM Journal on Scientific Computing*, 17(1):227–238, 1996. 6
- [44] Bruce Walter, Shuang Zhao, Nicolas Holzschuch, and Kavita Bala. Single scattering in refractive media with triangle mesh boundaries. In *ACM SIGGRAPH*, pages 1–8. ACM, 2009. 3
- [45] Haoran Wang, Nantheera Anantrasirichai, Fan Zhang, and David Bull. UW-GS: Distractor-aware 3d gaussian splatting for enhanced underwater scene reconstruction. In *IEEE/CVF Winter Conference on Applications of Computer Vision*, pages 1–10, 2025. 1, 6, 7, 8
- [46] Zhou Wang, A.C. Bovik, H.R. Sheikh, and E.P. Simoncelli. Image quality assessment: from error visibility to structural similarity. *IEEE Transactions on Image Processing*, 13(4): 600–612, 2004. 7
- [47] Zhiwen Yan, Chen Li, and Gim Hee Lee. Nerf-ds: Neural radiance fields for dynamic specular objects. In *Proceedings of the IEEE/CVF Conference on Computer Vision and Pattern Recognition*, pages 8285–8295, 2023. 2
- [48] Daniel Yang, John J Leonard, and Yogesh Girdhar. Seasplat: Representing underwater scenes with 3d gaussian splatting and a physically grounded image formation model. *arXiv preprint arXiv:2409.17345*, 2024. 1, 6, 7, 8
- [49] Richard Zhang, Phillip Isola, Alexei A. Efros, Eli Shechtman, and Oliver Wang. The unreasonable effectiveness of deep features as a perceptual metric. In *Proceedings of the IEEE Conference on Computer Vision and Pattern Recognition (CVPR)*, 2018. 7
- [50] Xiaoyu Zhou, Zhiwei Lin, Xiaojun Shan, Yongtao Wang, Deqing Sun, and Ming-Hsuan Yang. Drivinggaussian: Composite gaussian splatting for surrounding dynamic autonomous driving scenes. In *Proceedings of the IEEE/CVF Conference on Computer Vision and Pattern Recognition*, pages 21634–21643, 2024. 2
- [51] M. Zwicker, H. Pfister, J. van Baar, and M. Gross. Ewa volume splatting. In *Proceedings Visualization*, pages 29–538, 2001. 3
- [52] M. Zwicker, H. Pfister, J. van Baar, and M. Gross. Ewa splatting. *IEEE TVCG*, 8(3):223–238, 2002. 3